High Helmholtz Sound Prediction Generated by Confined Flows and Propagation within Ducts

Morteza Bayati and Mehran Tadjfar

Aerospace Engineering Department, Amirkabir University of Technology, Tehran 15875-4413, Iran

A hybrid method for the computation of noise radiation by a confined flow is used in this study. The proposed approach is appropriate and quite powerful for high Helmholtz numbers (i.e. when the turbulence/body interaction region is acoustically non-compact). The validation of this method is checked by comparing it with the analytical results of the tailored Green's function to the spinning of two vortex filaments in an infinite 2-D duct. The method is applied to the prediction of sound in a duct obstructed by a diaphragm. The sound sources generated by the fluctuations in the flow field are computed by means of an incompressible Large Eddy Simulation (LES). These sources are fed into a 2-D acoustic propagation Boundary Element Model (BEM). The predicted total acoustic power is 1.8 dB higher than the result obtained in the literature by Direct Numerical Calculation (DNC) and extrapolated experimental data for the same pipe configuration.

NOMENCLATURE

c_0	Sound speed
ϕ	Field variable
$()_0$	Reference quantities
u_i	Velocity components
$()_L$	Flow quantity
$()'$	Fluctuation
$()_a$	Acoustic quantity
n_i	Normal vector
δ_{ij}	Kronecker delta
T_{ij}	Lighthill tensor
H_0^1	Hankel function of the first kind
$C(x)$	Solid angle
x	Source position (vector $\vec{x}$)
y	Listener position (vector $\vec{y}$)
p	Pressure
V_ε	Exclusion volume
f	Frequency
δ_e	Momentum thickness
I	Acoustic intensity
P	Acoustic power
ω	Angular frequency ($\omega = 2\pi f$)
G	Green function

1. INTRODUCTION

In many practical applications, sound is generated by the interaction of turbulent flow with solid walls. In this situation, the sound wave experiences multiple reflections before propagation to a far field. Therefore, the sound spectrum exhibits rich frequencies content consisting of broadband and tonal components. To predict the acoustics field in these situations, a general aero-acoustic framework is required. More importantly, the employed method must often avoid many simplifying assumptions about geometry, compactness, or frequency content of sound sources.

The prediction of flow-induced noise requires accounting for the physics of both unsteady flow and the sound wave, simultaneously, since both are a solution of the compressible Navier-Stokes equation. The basic difficulties for such computations are numerous disparities between energies and length-scale in the turbulent flow and the sound field. Sound waves carry only a minuscule fraction of the flow energy, and a high-order numerical scheme is required to keep the sound wave intact. These fundamental differences are exacerbated in a low Mach number flow,[1] where the radiated acoustic power is smaller than the hydrodynamic flow power by roughly $O(M^4)$. In addition, the acoustic CFL number imposes extremely small time steps on the numerical solution in order to resolve both acoustics and hydrodynamics. That is why it is commonly accepted that hybrid methods are more appropriated for low Mach number flows. An example of a two-step or hybrid method for nearly incompressible flows is Lighthill,[2] who formally separated acoustics from hydrodynamics by introducing his acoustic analogy. It was shown that the flow mechanism that produced noise could be expressed in the form of equivalent sources in a uniform medium at rest, chosen as a representation of the propagation region surrounding the listener. The idea of equivalent sources has proven to be quite powerful at low Mach numbers. Curle[3] extended the Lighthill analogy to predict the sound of turbulent-body interaction by introducing a dipole source. Ffowcs Williams and Hawkings[4] generalized previous analogies to account for moving sources and the resulting Doppler effects.

Most of the works in literature are exterior problems. In the present work, we are concerned with the noise generated by confined flows and its propagation within the ducting. The interaction of pipe flow with singularities like diaphragm, valve contractions, or pipe junctions are sources of internal noise in industrial duct networks.[5,6] The problem of aerodynamics sound generation in pipes, allowing the aeroacoustics analogy by Davies and Ffowcs Williams,[7] showed that the acoustic efficiency of turbulence within a straight infinite duct varies with frequency from a dipole-like behaviour below the cut-off fre-

quency to free-field quadrupolar efficiency as soon as a few transverse modes are cut-on. Nelson,[8] Peters,[9] and Piellard[10] have focused on the prediction of noise generated by duct geometrical discontinuities.

Low frequencies are often considered,[11] which has two advantages: firstly, the source is acoustically compact; secondly, for frequencies below the duct cut-off, the one-dimensional Green's function can be employed. However, in many engineering products that contain ducts, the spectrum of interest often extends beyond the transverse cut-off frequency, up to several KHz. Mak[12] and Han and Mak[13] formulated the sound powers produced by the interaction of multiple in-duct elements at frequencies below and above the first transverse duct mode cut-on frequency.

The configuration of the present study corresponds to experiments of Van Herp et al.,[14] and the DNC result of Gloerfelt and Lafon.[15] The general scope of this work is to develop and validate a numerical tool for aeroacoustics noise prediction above the first cut-off frequency. This method is suitable for the determination of acoustic scattering by using an incompressible flow model in order to extend the applicability of Curle's analogy for non-compact and high Helmholtz numbers $He = 2\pi f D/c_0$. Schram[16] has shown that the derivation of a BEM variant of Curle is able to predict the aeroacoustics above the first cut-off frequency and could be employed for non-compact cases. A hybrid method was introduced for acoustic computation in the entire frequency range resolved by the flow solver for compact/non-compact sources. The flow-generated sound sources are computed using an LES solver. These sources are then used as the input data for the aeroacoustic solver, which is a boundary integral equation of Curle's analogy in the frequency domain, assuming a Hankel function as the 2-D Green's function that was solved using a boundary element method introduced by Khalighi and Bodony.[17]

The paper is organized as follows: first a derivation of the BEM variant of Curle's analogy is given, and then validation studies of this method for the spinning of two vortex filaments in an infinite straight duct for non-compact high Helmholtz numbers are put forth. Finally, we demonstrate the applicability of the method to engineering problems by computing the sound of internal confined flow through a diaphragm in a duct.

2. METHODOLOGY

An acoustic analogy for the prediction of the acoustics field radiation by an unsteady flow consists of a forced wave equation:

$$\left(\nabla^2 - \frac{1}{c_0^2}\frac{\partial^2}{\partial t^2}\right)\phi(x,t) = q(x,t); \qquad (1)$$

where c_0 is the sound speed, and ϕ is a field variable, which can be the pressure or the density perturbation. Subscript $()_0$ denotes the reference quantities. The source q can be estimated independently by an exact recombination of the continuity and momentum equations which yield to:

$$q = -\frac{1}{c_0^2}\frac{\partial^2 T_{ij}}{\partial x_i \partial x_j}; \qquad (2)$$

in which $T_{ij} = \rho u_i u_j + (p' - c_0^2\rho')\delta_{ij} - \sigma_{ij}$ defines the Lighthill tensor in terms of velocity components u_i, Reynolds stresses,

non-isentropic processes, and viscous stresses σ_{ij}. If we consider duct configurations with a high enough Reynolds number for the acoustic contribution of the wall-normal dipoles to dominate over the viscous stresses and for low Mach numbers, the convection and refraction of the sound wave is negligible compared to the scattering by duct geometry.

By implementing these assumptions, the wave propagation equation is integrated in time and space and after convolution by Green's function $G(t, x|\tau, y)$, the following is defined:

$$\rho'(x,t) = \int_{-\infty}^{t}\iiint_V \frac{\partial^2 T_{ij}}{\partial y_i \partial y_j}G\,d^3y\,d\tau -$$

$$c_0^2\int_{-\infty}^{t}\iiint_V\left(\rho'\frac{\partial^2 G}{\partial y_i^2} - G\frac{\partial^2\rho'}{\partial y_i^2}\right)d^3y\,d\tau +$$

$$\int_{-\infty}^{t}\iiint_V\left(\rho'\frac{\partial^2 G}{\partial \tau^2} - G\frac{\partial^2\rho'}{\partial \tau^2}\right)d^3y\,d\tau; \qquad (3)$$

which would consist of treating the turbulent field as a monopole. A more appropriate formulation is obtained by performing integration by part of the volume integral of Eq. (3) to highlight the quarupolar character of free turbulence. The third integral of Eq. (3) vanishes by virtue of causality after integration by part. This yields:

$$\rho'(x,t) = \int_{-\infty}^{t}\iiint_V T_{ij}\frac{\partial^2 G}{\partial y_i \partial y_j}\,d^3y\,d\tau -$$

$$\int_{-\infty}^{t}\iint_{\partial V}\left(c_0^2\frac{\partial\rho'}{\partial y_i}G + (p' - c_0^2\rho')\frac{\partial G}{\partial y_i}\right)n_i\,d^2y\,d\tau -$$

$$c_0^2\int_{-\infty}^{t}\iint_{\partial V}\left(\rho'\frac{\partial G}{\partial y_i} - G\frac{\partial\rho'}{\partial y_i}\right)n_i\,d^2y\,d\tau. \qquad (4)$$

The free-field Green's function:

$$G(x,t|y,\tau) = \frac{\delta(t - \tau - |x-y|/c_0)}{4\pi c_0^2|x-y|} \qquad (5)$$

is used in Eq. (4).

A crucial step in the derivation of Curle's analogy is the cancellation of the scattering integral with the density perturbation term of the second integral in Eq. (4). This yields the classical result:

$$\rho'(x,t) = \int_{-\infty}^{t}\iiint_V T_{ij}\frac{\partial^2 G}{\partial y_i \partial y_j}\,d^3y\,d\tau -$$

$$\int_{-\infty}^{t}\iint_{\partial V} p'\frac{\partial G}{\partial y_i}n_i\,d^2y\,d\tau. \qquad (6)$$

The pressure of the solid boundary appears through the dipole source. The derivation of Curle's analogy assumes that the flow model used to quantify the equivalent sources accounts for compressibility effects, including acoustic scattering. This, however, is usually not the case for a low Mach number, for which incompressible flow modelling is much more

efficient and, therefore, preferred. The analogy is valid for a low Helmholtz number or for a compact case for which acoustical effects can be approximately described by an incompressible model. For high Helmholtz numbers, the incompressible flow model must be complemented by an acoustic correction to obtain a realistic sound. For an idealized case, the analytical tailored Green's function with zero normal gradients at the boundary surface can correct the acoustic sound prediction, but in most industrial applications and ranges of frequencies, the problem is not amenable to an analytical solution. For internal problems, combining Curle's analogy with the boundary element method brings the acoustical correction when using an incompressible flow model.

To do this, we start from the inhomogeneous wave propagation equation in the Fourier domain, which takes the form of the Helmholtz equation:

$$\nabla^2 \hat{p}_a + k^2 \hat{p}_a = \hat{q}; \qquad (7)$$

where $k = \omega/c_0$ is the wave number, and $\hat{q} = \frac{\partial^2 \hat{T}_{ij}}{\partial x_i \partial x_j}$ is the Lighthill tensor. In what follows, the hat notation indicating the Fourier component will be dropped for the sake of readability.

Convoluting Eq. (7) with a free-field Green's function yields:

$$\iiint\limits_{V \backslash V_\varepsilon} \left(\nabla^2 p_a G - p_a \nabla^2 G \right) d^3 y =$$
$$\iiint\limits_{V \backslash V_\varepsilon} q_L G \, d^3 y + \iiint\limits_{V \backslash V_\varepsilon} p_a \delta(x - y) \, d^3 y. \qquad (8)$$

In Eq. (8), the appropriate Fourier domain free-field Green's function is $G = \exp(-ikr)/(4\pi r)$ for the three-dimensional, and the Hankel function of the first kind $G = \frac{i}{4} H_0^1(kr)$ for the two-dimensional simulation. At this, $r = |x - y|$ is the distance between the source point to listener position.[18] Subscript $(\,)_L$ has been added to quantities that are provided through the flow and subscript $(\,)_a$ to signify acoustic quantity.

In the derivation of Curle's analogy, the listener is defined well apart from the source field at a uniform and quiescent region. On the contrary, the resolution of the boundary integral equation is performed by collocation (i.e. by placing the listener on the source region). The singularity is excluded by removing an exclusion volume V_ε at Eq. (8). Its contribution will be evaluated by letting the exclusion volume shrink to zero. The point x is excluded from the integration volume $V \backslash V_\varepsilon$, therefore the third integral of Eq. (8) is zero.

Applying the Green theorem and integration by parts yields:

$$C(x)P_a(x) = \iiint\limits_V T_{ij} \frac{\partial^2 G}{\partial y_i \partial y_j} \, d^3 y +$$
$$\iint\limits_{\partial V} \left(-c_0^2 \frac{\partial \rho_L}{\partial n} G - (p_L - c_0^2 \rho_L) \frac{\partial G}{\partial n} \right) d^2 y -$$
$$C(x)(p_L - c_0^2 \rho_L) + \iint\limits_{\partial V} \left(\frac{\partial p_a}{\partial n} G - p_a \frac{\partial G}{\partial n} \right) d^2 y. \qquad (9)$$

Factor $C(x)$ is the solid angle equal to 1 when x is within the volume and equal to $\frac{1}{2}$ when x lies over a smooth surface and is equal to zero elsewhere. From the compressibility effects, we have $c_0^2 \rho_L = p_a$ and Eq. (9) becomes:

$$C(x)P_L(x) = \iiint\limits_V T_{ij} \frac{\partial^2 G}{\partial y_i \partial y_j} \, d^3 y - \iint\limits_{\partial V} p_L \frac{\partial G}{\partial n} \, d^2 y. \qquad (10)$$

Equation (10) is fairly similar to the classical analogy of Curle,[6] with some differences related to the change from the time domain to the frequency domain, including the factor c_0^2 due to a different Green's function in the time and frequency domains. At Eq. (6), which is the analogy of Curle, the listener is often assumed to be in a uniform and quiescent propagation region well apart from the sound production region. That is usually employed to obtain the acoustic component only while Eq. (10) yields the full-pressure fluctuation, hydrodynamic, and acoustic pressure. This results from allowing the listener to enter the source domain, unlike the Curle's analogy.

For high Helmholtz numbers, the case would be non-compact, and with low Mach numbers, the incompressible flow is preferred, and Eq. (10) yields erroneous results, as shown by Schram.[19] In a general case, the pressure is expressed as a sum of hydraulic and acoustic components:

$$p_L = p_h + p_a. \qquad (11)$$

Also, the integration domain is decomposed in two parts, corresponding respectively to volume V_1 and V_2 and their boundaries ∂V_1 and ∂V_2. The domain V_1 is localized around the collection point x with dimensions acoustically compact. The solution of Eq. (10) can resolve the hydrodynamic part of pressure p_L. The domain V_2 is defined as $v \backslash V_1$. The substitution of Eq. (11) into Eq. (10) and subtracting the hydrodynamic pressure of domain V_1 yields:

$$C(x)P_a(x) = -\iint\limits_{\partial V_1} p_a \frac{\partial G}{\partial n} \, d^2 y + \iiint\limits_{V_2} T_{ij} \frac{\partial^2 G}{\partial y_i \partial y_j} \, d^3 y -$$
$$\iint\limits_{\partial V_2} (p_h + p_a) \frac{\partial G}{\partial n} \, d^2 y$$
$$= -\iint\limits_{\partial V} p_a \frac{\partial G}{\partial n} \, d^2 y + \iiint\limits_{V_2} T_{ij} \frac{\partial^2 G}{\partial y_i \partial y_j} \, d^3 y -$$
$$\iint\limits_{\partial V_2} p_h \frac{\partial G}{\partial n} \, d^2 y; \qquad (12)$$

where the boundary integrals involving the acoustic pressure p_a have been grouped together. The wall pressure is the sum of the hydrodynamic component from an incompressible flow model and an acoustical component, which is the solution of Eq. (12).

From the boundary element solution[20] of Eq. (12), the first resolved acoustic component of wall pressure then must be summed up with hydrodynamic pressure to give the total dipole source of Eq. (6). The classic formulation of Eq. (6) is used to obtain the acoustic field at the listener's position in the propagation region.

3. VALIDATION

The acoustic pressure calculated by the hybrid approach is validated against the analytical solution of the tailored Green's function.[19,21] The benchmark is a two-dimensional case of two filament vortices spinning within an infinite duct with height h. Through the simplicity of this test cast, both the flow and acoustic field along the duct can be derived from an analytical calculation. The sound prediction is obtained in two ways. The first approach consists of using the tailored Green's function built from the duct mode.[7] This approach provides the reference solution. The second method is our hybrid formulation, using a free-field Green's function, which it is the Hankel function of the first kind. The quadrupole source terms and unsteady hydrodynamic pressure are obtained from an analytical derivation from the vortex model. An incompressible flow description is derived from the Biot-Savart induction of the two spinning vortices by a distance of $h/2$. The relevant Mach number is 0.5 with a speed of sound of $c_0 = 340$ ms^{-1}. The velocity formula of the computational domain and the trajectories of the two vortices and unsteady pressure distribution at the wall are formulated in Appendix A.

The simplicity of this configuration allows for the analytical solving of the 2-D Helmholtz equation:

$$\nabla^2 G_1 + k^2 G_1 = \delta(x - x_0)\delta(y - y_0). \tag{13}$$

With boundary condition $\partial G/\partial n = 0$, the 2-D tailored Green's function G_1 can be expressed as an infinite sum over the duct modes:

$$G_1(x, y|x', y') = \frac{i}{h} \sum_{n=0}^{\infty} \frac{1}{k_n} \cos\left(\frac{n\pi y}{h}\right) e^{\mp i k_n (x-x')} \cos\left(\frac{n\pi y'}{h}\right). \tag{14}$$

With $k_n = \left(k^2 - \mu_n^2\right)^{\frac{1}{2}}$, $\mu_n = n\pi y/h$ and the $-$ and $+$ sign correspond to waves propagating, respectively to the right and left from the source. Substituting the tailored Green's function Eq. (14) into Eq. (13) yields the acoustic pressure:

$$
\begin{aligned}
P_a(x, y, \omega) &= \iiint_V T_{ij} \frac{\partial^2 G}{\partial x' \partial y'} \, dx' dy' \\
&= \frac{1}{h} \iint_{\partial V} \sum_{n=0}^{\infty} e^{\mp i k_n (x-x')} \cos\left(\frac{n\pi y}{h}\right) \\
&\quad \left\{ -i k_n \cos\left(\frac{n\pi y'}{h}\right) T_{11}(x', y', \omega) - \right. \\
&\quad \frac{i\pi^2 n^2}{h^2 k_n} \cos\left(\frac{n\pi y'}{h}\right) T_{22}(x', y', \omega) \pm \\
&\quad \left. \frac{2\pi n}{h} \sin\left(\frac{n\pi y'}{h}\right) T_{12}(x', y', \omega) \right\} dx' dy'.
\end{aligned} \tag{15}
$$

The series is truncated beyond a sufficient number of evanescent modes. Equation (15) is an exact solution of the ducted vortex spinning problem.

The duct extends in the axial direction between $x/h = -5$ and 5, and has a unit height $h = 1$. The first cut-on frequency in the x-direction corresponds to the Helmholtz number $He = \pi$, and the second cut-on is 2π. An acoustical impedance boundary condition $Z = \rho_0 c_0$ at both ends of the
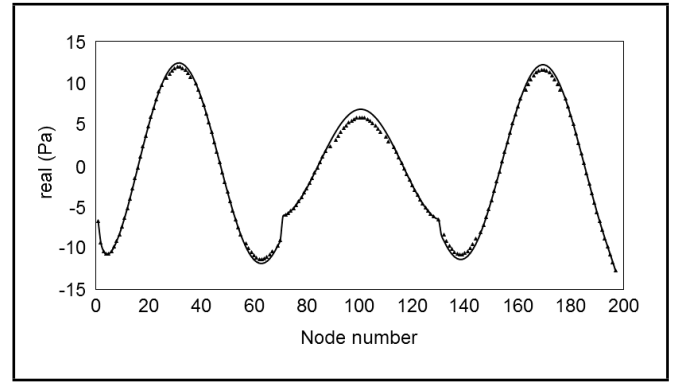

Figure 1. The real part of acoustical pressure at the upper wall of the duct, $He = 2$; ▲ exact solution; — hybrid method.
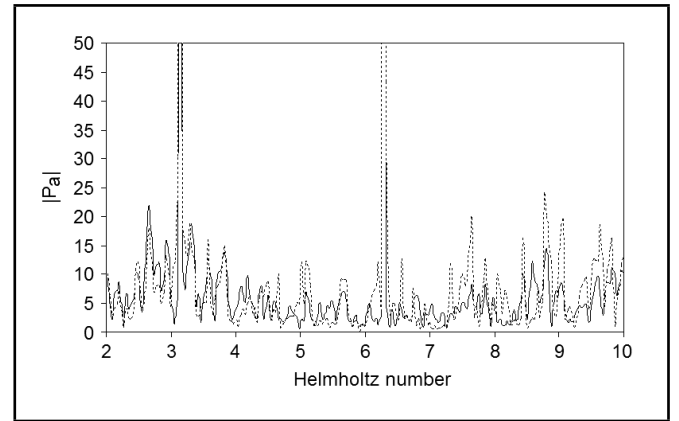

Figure 2. Acoustical pressure evaluated at a listener position $(x/h, y/h) = (2.025, 0.175)$. — exact solution; - - - hybrid method.

duct is applied to have non-reflection boundary conditions at the hybrid numerical method in order to permit comparison with the infinite duct reference solution. Figure 1 shows the real acoustic pressure at the upper wall from the hybrid and exact numerical solutions at the Helmholtz number equal to $He = 2$. The hybrid method covers the results of the exact solution.

The acoustic pressure from the hybrid method and the analytical method are compared for frequencies covering the range of the Helmholtz number from 1 to 10. Figure 2 shows the acoustical pressure calculated from hybrid and exact methods at the coordinate of (2.025, 0.175). At frequencies below the first transverse duct mode, as shown in Fig. 1, the hybrid method results are very close to the results of the analytical solution. By increasing the frequency to above the frequency of the first and second transverse duct modes, the accuracy of the hybrid sound prediction method will begin to deteriorate as shown in Fig. 2. The acoustic pressure contours below and above the cut-on frequencies, and Helmholtz numbers of 2, 2.4, and 4.8 are presented respectively in Fig. 3, where the results from the hybrid method and the exact solution are compared.

Figure 1 and Fig. 3(a) are at $He = 2$, where the hybrid method is in excellent agreement with the results of the exact solution. However at $He = 2.4$, some difference can be observed, and at $He = 4.8$ the differences increase, but the comparison is still acceptable. Hence, by comparing the results of the hybrid method to that of the exact solution of this test
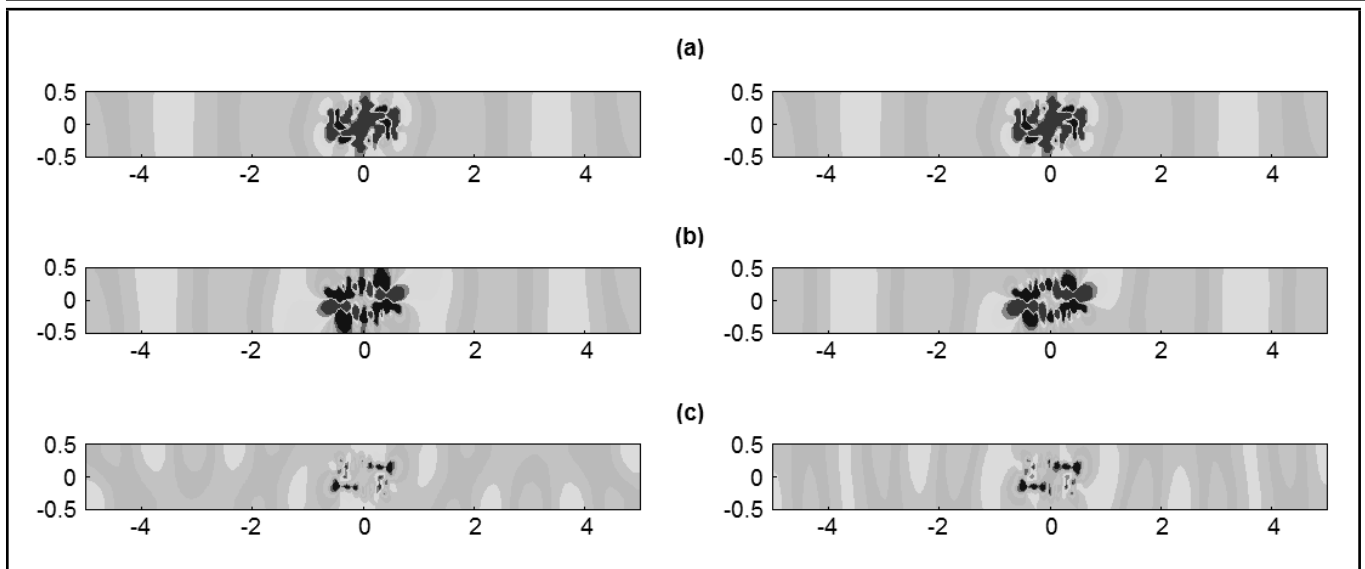
Figure 3. Imaginary part of acoustic pressure at Helmholtz number: (a) $He = 2$, (b), $He = 2.4$, (c) $He = 4.8$. Left column: hybrid method, right column: exact method; levels between -16 and 16.

case, the reliability of this hybrid method can be concluded. For industrial applications, the geometries and problems are sufficiently complicated so that the analytical formulation cannot be performed to derive an exact solution of the problems. Therefore, using the hybrid approach is forced. In this work, we utilize our hybrid solution of the sound wave equation for the prediction of sound generated by a diaphragm through a duct. Since the flow field is also quite complicated, a computational fluid dynamic is needed to simulate the flow through the diaphragm. In this way, we can compute the sound source terms needed in the acoustic calculations. In order to accurately predict the flow quantities, such as the velocities and pressure fluctuations, Large Eddy Simulation (LES) is the most feasible choice.

4. SOUND GENERATION

This section presents the applicability of the hybrid method to the computation of noise by a turbulent flow through a diaphragm in a duct at low Mach numbers. Direct noise computation for flow over this configuration was carried by Gloerfelt and Lafon.[15] The source fluctuations in the flow are first computed by a Large Eddy Simulation (LES) of an incompressible fluid with the Dynamic Smagorinsky Model,[22–24] and then they are fed to the following hybrid acoustical computation as input data.

4.1. Governing Equation

The flow field is computed with a three-dimensional incompressible Large Eddy Simulation (LES) using a finite-volume code to simulate the aerodynamic field. The underlying numerical scheme consists of a fully conservative second-order FV space discretization with a collocated arrangement of variables on a non-orthogonal grid. For the time discretization, an implicit second-order scheme is employed, while a non-linear multi-grid scheme, in which the pressure correction method acts smoother on the different grid levels, is used for convergence acceleration. In LES, the flow field is decom-

posed into a large-scale or grid scale (GS) component and a sub-grid scale (SGS) component, given for a field variable $\phi = (\overline{\phi})_{\text{GS}} + (\phi')_{\text{SGS}}$.

The GS component is obtained by filtering the entire domain using a grid filter function. The filtering operation removes the SGS turbulence from the Navier-Stokes equation. The resulting governing equations are then solved directly for the GS turbulence motions, while the effect of the SGSs is computed using an SGS model, such as the classical Smagorinsky model used in this work.[22]

The governing equations of the LES are spatially filtered as:

$$\frac{\partial \overline{u}_i}{\partial x_i} = 0; \tag{16}$$

$$\frac{\partial \overline{u}_i}{\partial t} + \frac{\partial}{\partial x_j}\left(\overline{u}_i \overline{u}_j + \tau_{ij}\right) = -\frac{1}{\rho}\frac{\partial p}{\partial x_i} + \frac{\partial}{\partial x_j}\left\{\nu\left(\frac{\partial \overline{u}_i}{\partial x_j} + \frac{\partial \overline{u}_j}{\partial x_i}\right)\right\}; \tag{17}$$

where u and p are the grid-scale components, and ν is the kinematics' viscosity. The viscous stress tensor τ_{ij} is modelled as a Newtonian fluid $\tau_{ij} = 2\mu S_{ij}$, where μ is the dynamic molecular viscosity, and S_{ij} is the deviatoric part of the deformation stress tensor. The sub-grid scale (SGS) stress tensor τ_{ij} is defined by:

$$\tau_{ij} = \overline{u_i u_j} - \overline{u}_i \overline{u}_j. \tag{18}$$

The Smagorinsky closure is applied to the SGS stress τ_{ij}:

$$\tau_{ij} - \frac{1}{3}\delta_{ij}\tau_{kk} = -2\nu_{\text{SGS}}\overline{S}_{ij}; \tag{19}$$

where $\nu_{\text{SGS}} = (C_s\Delta)^2|\overline{S}|$, $|\overline{S}| = \sqrt{2\overline{S}_{ij}\overline{S}_{ij}}$, $\overline{S}_{ij} = \frac{1}{2}\left(\frac{\partial \overline{u}_i}{\partial x_j} + \frac{\partial \overline{u}_j}{\partial x_i}\right)$.

The quantity Δ is the size of the grid filter and C_s is the Smagorinsky coefficient that is computed with the Dynamic Smagorinsky Model (DSM) where modification by Lilly is
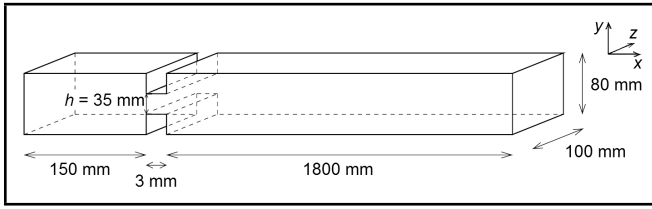
Figure 4. Computation domain.

used:

$$C_s = \frac{1}{2} \frac{\langle M_{ij} L_{ij} \rangle}{\langle M_{ij} L_{ij} \rangle}; \tag{20}$$

$$M_{ij} = \widetilde{\Delta}^2 |\widetilde{\overline{S}}| \widetilde{\overline{S}}_{ij} - \overleftarrow{\Delta^2 |\overline{S}| \overline{S}_{ij}}; \tag{21}$$

$$L_{ij} = \overleftarrow{\widetilde{\overline{u}}_i \overline{u}_j} - \widetilde{\overline{u}}_i \widetilde{\overline{u}}_j. \tag{22}$$

The symbol '$\sim$' represents a test filtering operation where $\widetilde{\Delta}/\Delta \approx 2$ and '$\langle \rangle$' represent an averaging operation. The filter is the Laplacian operation.[25] The chosen configuration was shown in Fig. 4.

The cross-sectional area $h_c \times l_c = 80 \times 100$ mm^2. The slip-shaped aperture of the diaphragm has a height, $h = 35$ mm, and spans the transverse width of the duct. The mesh used is a non-uniform Cartesian grid with 813,500 cells. The diaphragm is located at the 42nd grid point in the x-direction and extends over 15 points horizontally and 19 points vertically. The duct length downstream the diaphragm is then at 1.8 m. The grid is refined near the rectangular aperture and then stretched with the rate of 6%. The grid in the y-direction is uniform over the diaphragm aperture with $\Delta y = 2$ mm. The mesh size in the span-wise z-direction is $\Delta z = 2$ mm. A CFL number of 0.9 and $\Delta x_{min} = 0.375$ mm near the rectangular aperture leads to a time step $\Delta t = $ CFL $\times \Delta x_{min}/c_0 = 9.75 \times 10^{-7}$ s. Approximately 200,000 time steps (i.e. 0.2 s of physical time) are performed. The inlet velocity is 6 ms^{-1} and the Reynolds number based on the height of the diaphragm is $Re_h = 14000$. The Reynolds number based on the height of the duct is $Re_h = 33000$. The cut-off frequency according to a maximum mesh size of $\Delta x_{max} = 18$ mm at the outlet is about 2500 Hz.

The flow parameters used in the experimental setup[14] are $p_\infty = 10^5$ Pa, $\rho_\infty = 1.168$ kg/m^3, $c_\infty = 346.15$ m/s, which are the freestream pressure, density, and sound speed, respectively. The kinematic viscosity of the air is $\nu_\infty = 1.46 \times 10^{-5}$ m^2/s.

The component of the average velocities in Fig. 5 illustrates that the flow through the diaphragm can be separated into three regions: first, the uniform flow in the upstream duct, second, the jet-type flow emanating from the diaphragm where most acoustic energy is produced, and third, the uniform flow in the downstream duct segment after $x = 0.4$ m.

An asymmetric flow, in spite of the symmetric test section and symmetric inlet and outlet, called the Coanda effect[26] occurred in this case. An increase of velocity near one wall is accompanied with a decrease in the pressure, and then a pressure difference is established across the duct, this will maintain the asymmetry of the flow. This break in the symmetry can be associated to a pitchfork bifurcation. At lower Reynolds numbers, experiments and stability analyses show that a constricted channel has a unique symmetric solution below a prescribed
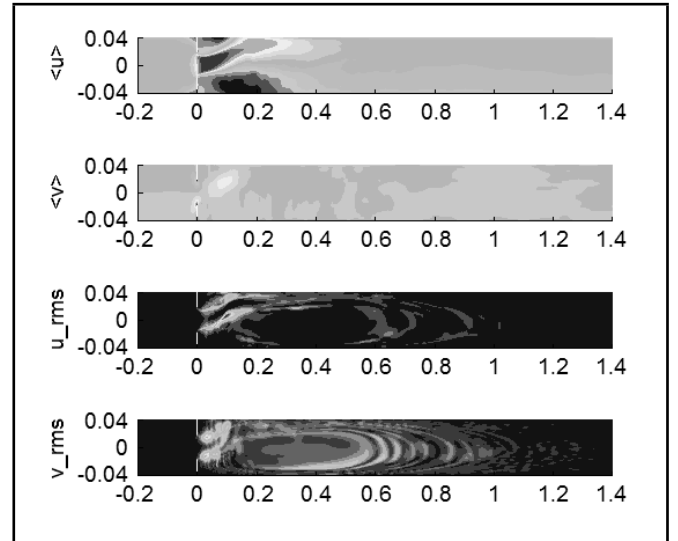

Figure 5. Average velocities $\overline{u}$ (levels between -10 and 20 m/s), $\overline{v}$ (levels between –7 and 7 m/s), u_{rms} (levels between 0 and 7 m/s), and v_{rms} (levels between 0 and 5 m/s).

Reynolds number, dependent on the contraction ratio and on the shape of the contraction. Above this critical Reynolds number, a pitchfork bifurcation results in a stable asymmetric flow. In the present simulation, the reattached point from the jet was about $x = 170$ mm at the upper wall. For comparison, an attachment point was near $x = 175$ mm in the work of Gloerfelt,[15] and an attachment point near $x = 150$ mm has been measured by particle image velocimetry (PIV) for the same geometry but with an incoming velocity of 14 m/s.[27] The choice of one side or the other is dependent on the subtle details of the initialization and transient history of the flow, which can place the flow in the domain of attraction of one or the other solutions in the multidimensional state space.

Power Spectral Densities (PSD) of vertical velocity at several locations in the upper shear layer are shown in Fig. 6. Data are evaluated for 2400 samples with a resolution of $\Delta f = 10.6$ Hz and a sampling rate of 25 kHz. The similarity parameter $\eta = (y - y_{0.5})/\delta_\theta$ shows that the mean stream-wise velocity profiles collapse for $\delta_\theta = 1$ mm instead of 0.7 mm[15] (See Fig. 7). This momentum thickness corresponds to the Strouhal number $St_{\delta_\theta} = f\delta_\theta/U_m$ equal to 0.019, close to the value of 0.017 for the most unstable frequency of a hyperbolic tangent velocity profile in the linear stability analysis.[28] In the similarity parameter, $y_{0.5}$ corresponds to $\overline{u} = 0.5U_m$ and U_m is 19 m/s at different longitudinal locations.

A peak centred around the Strouhal number 0.019 corresponding to the frequency 368 Hz is presented at $(x, y, z) = (0.04, 0.01, 0.0)$. This peak therefore indicates the presence of Kelvin-Helmholtz instability in the jet shear layer. Other points exhibit a more broadband content correlating to the periodic shedding and collapse of large-scale jet column instabilities.

4.2. Acoustic Simulation

At a 2-D slice of the duct, in the central plane of the diaphragm, the acoustic pressure was computed with the hybrid method. An acoustic computation is performed based on the acoustic source terms computed by LES simulation. Since
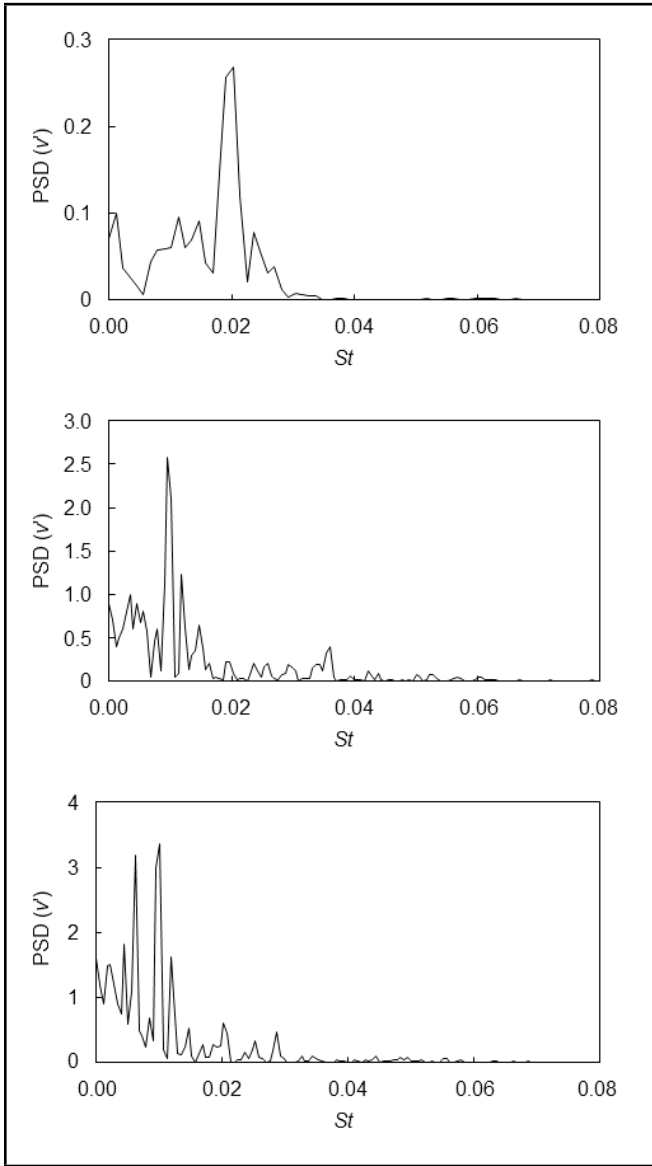
Figure 6. PSD of instantaneous vertical velocity fluctuations v' in m^2/s^2/Hz vs. Strouhal number. From top to bottom, measured points located at $y = 0.01$, $z = 0$, $x = 0.04$, 0.12, and 0.16.

the flow field is simulated as three-dimensional, the acoustic source terms are calculated at the central surface of the duct in the xy plane. Then they are fed to the aeroacoustic solver code for the prediction of the noise generated by the turbulence flow inside a duct.

Spatial filtering[29] according to Eq. (23) is applied to the smooth source outgoing from the source region.

$$w(x) = \begin{cases} 1 & x \le x_1 \\ 1 - \frac{x - x_1}{L_1} & x > x_1 \end{cases} ; \qquad (23)$$

where x_1 is defined as the position from which the weighting is applied, and L_1 is the length of the subdomain where the weighting is applied.

The acoustic power is obtained from acoustic intensity I in the outlet section of the duct:

$$P_{\text{dB}} = 10 \log \left(\frac{I}{I_{\text{ref}}} \times S \right) \qquad (24)$$

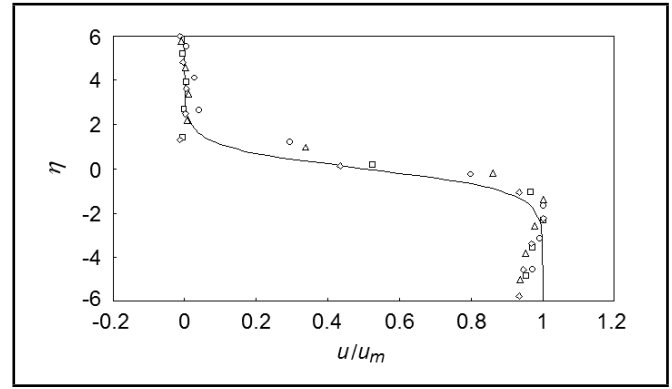$$I = \frac{1}{\rho_0 C_0} \int \left[\text{PSD}(p') \right](f) \, df; \qquad (25)$$

Figure 7. Mean streamwise velocity profiles. — hyperbolic tangent profile $(1-\tanh)/2$, □: $x = 1.5$ mm, ◇: $x = 3$ mm, △: $x = 6$ mm, ○: $x = 9.5$ mm.
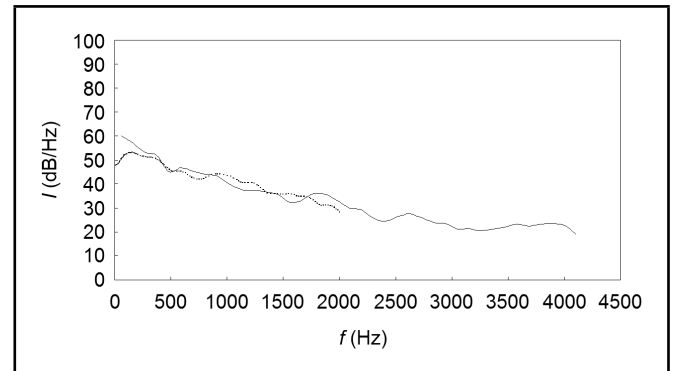

Figure 8. Power spectral at the outlet section. - - - DNC result,[15] — hybrid method.

where $I_{\text{ref}} = 10^{-12}$ Wm^2. At the inlet and outlet of the duct, the acoustic power is equal to 71.5 dB and 80.3 dB, respectively, which are close to the 69 dB and 78.8 dB from the DNC result of Gloerfelt and Lafon.[15] The total acoustic power is obtained by summing the acoustic intensities in the inlet and outlet sections. From our hybrid method of prediction of sound, the total radiated power 80.8 dB are calculated, that the value of 79 dB was referred in the work of Gloerfelt[15] and 79.3 dB in the empirical U^4 law based on the experimental work of Van Herpe.[14] The power acoustic result predicted by the hybrid method at the outlet boundary is compared with the DNC results in Fig. 8. The measured power spectrum is an average of ten samples. The DNC result only exists up to a frequency equal to 2000 Hz, which is lower than 2163 Hz, which is the cutting frequency associated to the duct height, D.

The acoustic pressure maps in the computational domain of the diaphragm are shown in Fig. 9. This shows the imaginary part of the acoustic pressure in the Fourier domain at above and below the first frequency of the cut-off mode in the ducted diaphragm. Figure 9(a) is at $f = 2000$ Hz, which is below the cut-off frequency, and Fig. 9(b) shows the imaginary part of the acoustic pressure at $f = 3500$ Hz, which is above the cut-off frequency. The change in the formation of the acoustic pressure map below and above the first transverse mode of the duct is clearly obvious at Fig. 9. The acoustic pressure contours corresponding to the imaginary part of the acoustic pressure contours for the straight duct were shown in Fig. 3.
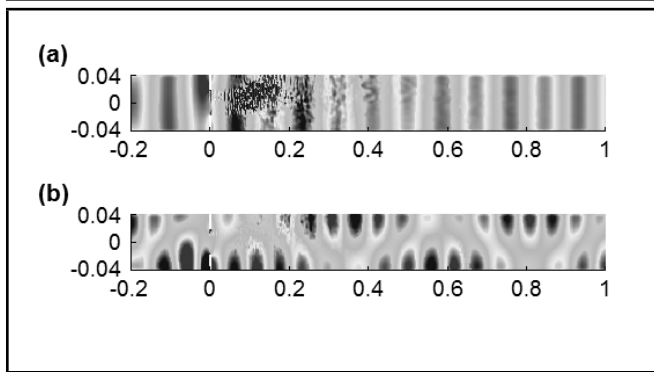
Figure 9. Imaginary part of acoustic pressure at: (a) $f = 2000$ Hz, (b) $f = 3500$ Hz. Levels between -0.002 and $+0.002$.

5. CONCLUSIONS

This work proposes a hybrid method that consists of an incompressible flow solver and boundary element method (BEM) for accurate prediction of sound generated by complex flows at low Mach numbers.

This approach was carefully validated for two spinning vortex filaments in an infinite two-dimensional duct. The results show excellent agreement between the hybrid method and the analytical acoustic field.

The proposed approach can predict the acoustic field in geometries of arbitrary extent and complexity, compact or non-compact, and high Helmholtz numbers.

As a demonstration of an engineering application, the sound generation over a diaphragm, which is applicable in heating, ventilating, and air-conditioning (HVAC) systems of automotive industries, was studied. The result of the hybrid approach was in good comparison with the DNC results in the frequency range adequately resolved by the numerical method.

REFERENCES

[1] Crighton, D. G. Computational aeroacoustics for low Mach number flows, *Computational Acoustics*, J. C. Hardin, M. Y. Hussaini (Eds.), Springer, New York, (1992), 50–68.

[2] Lighthill, M. J. On sound generated aerodynamically: I. General theory, *Proceedings of the Royal Society A*, **221**, 564–587, (1952).

[3] Curle, N. The influence of solid boundaries upon aerodynamic sound, *Proceedings of the Royal Society A*, **231**, 505–514, (1955).

[4] Ffowcs Williams, J. E., Hawkings, D. L. Sound generated by turbulence and surfaces in arbitrary motion, *Philosophical Transactions of the Royal Society A*, **264**, 321–342, (1969).

[5] Ryu, J., Cheong, C., Kim, S., Lee, S. Computation of internal aerodynamic noise from a quick-opening throttle valve using frequency-domain acoustic analogy, *Applied Acoustics*, **66**, 1278–1308, (2005).

[6] Yasuda, T., Wua, Ch., Nakagawa, N., Nagamura, K. Predictions and experimental studies of the tail pipe noise of

an automotive muffler using a one dimensional CFD model, *Applied Acoustics*, **71**, 701–707, (2010).

[7] Davies, H. G., Ffowcs Williams, J. E. Aerodynamic sound generation in a pipe, *Journal of Fluid Mechanics*, **32**, 765–778, (1968).

[8] Nelson, P. A., Morfey, C. L. Aerodynamic sound production in low speed ducts, *Journal of Sound and Vibration*, **79**, 263–289, (1981).

[9] Peters, M. C. A. M., Hirschberg, A. Acoustically induced periodic vortex shedding at sharpedged open channel ends: Simple vortex models, *Journal of Sound and Vibration*, **161**, 281–299, (1993).

[10] Piellard, M., Bailly, C. Several computational aeroacoustics solutions for the ducted diaphragm at low Mach number, *16th AIAA/CEAS Aeroacoustic Conference*, AIAA paper 2010–3996, (2010).

[11] Venkatesham, B., Tiwari, M., Munjal, M. L. Prediction of breakout noise from a rectangular duct with compliant walls, *International Journal of Acoustics and Vibration*, **16** (4), 180–190, (2011).

[12] Mak, C. M. A prediction method for aerodynamic sound produced by multiple elements in air ducts, *Journal of Sound and Vibration*, **287**, 395–403, (2005).

[13] Han, N., Mak, C. M. Prediction of flow-generated noise produced by acoustic and aerodynamic interactions of multiple in-duct elements, *Applied Acoustics*, **69**, 566–573, (2008).

[14] Van Herp, F., Crighton, D. G., Lafon, P. Noise generation by turbulent flow in a duct obstructed by a diaphragm, *16th Aeroacoustic Conference*, AIAA paper 95–035, (1995).

[15] Gloerfelt, X., Lafon, P. Direct computation of the noise induced by a turbulent flow through a diaphragm in a duct at low Mach number, *Computers & Fluids*, **37**, 388–401, (2008).

[16] Schram, C. A boundary element extension of Curle's analogy for non-compact geometry at low Mach number, *Journal of Sound and Vibration*, **322**, 264–281, (2009).

[17] Khalighi, Y., Bodony, D. J. Improved near-wall accuracy for solution of the Helmholtz equation using the boundary element method, *CTR Annual Research Briefs*, 313–322, (2006).

[18] Gloerfelt, X., Perot, F., Bailly, C., Juve, D. Flow induced cylinder noise formulated as a diffraction problem for low Mach numbers, *Journal of Sound and Vibration*, **287**, 129–151, (2005).

[19] Schram, C., Anthoine, J., Hirschberg, A. Calculation of sound scattering using Curle's analogy for non-compact bodies, *11th AIAA/CEAS Aeroacoustic Conference*, AIAA paper 2005–2836, (2005).

[20] Von Estorff, O. *Boundary Elements in Acoustics: Advances and Applications*, WIT Press, (2000).

[21] Dowling, A. P., Ffowcs Williams, J. E. *Sound and Sources of Sound*, Ellis Horwood, (1983).

[22] Smagorinsky, J. General circulation experiments with the primitive equations I. The basic experiment, *Monthly Weather Review*, **91**, 99–164, (1963).

[23] Germano, M., Piomelli, U., Moin, P., Cabot, W. H. A dynamic subgrid-scale eddy viscosity model, *Physics of Fluids A*, **3**, 1760–1765, (1991).

[24] Lilly, D. K. A proposed modification of the Germano subgrid-scale closure method, *Physics of Fluids A*, **4**, 633–635, (1992).

[25] Kato, C., Yamade, Y., Wang, H., Guo, Y., Miyazawa, M., Takaishi, T., Yoshimura, S., Takano, Y. Numerical prediction of sound generated from flows with a low Mach number, *Computers & Fluids*, **36**, 53–68, (2007).

[26] Cherdron, W., Durst, F., Whitelaw, J. H. Asymmetric flows and instabilities in symmetric ducts with sudden expansion, *Journal of Fluid Mechanics*, **84**, 13–31, (1978).

[27] Crouzet, F., Lafon, P., Buchal, T., Laurence, D. Aerodynamic noise prediction in internal flows using LES and linear Euler equations, *8th AIAA/CEAS Aeroacoustic Conference & Exhibit*, AIAA paper 2002–2568, (2002).

[28] Danaila, I., Dusek, J., Anselmet, F. Coherent structures in a round, spatially evolving, unforced, homogeneous jet at low Reynolds numbers, *Physics of Fluids*, **9**, 3323–3342, (1997).

[29] Oberai, A. A., Roknaldin, F., Hughes, T. J. R. Computational procedures for determining structural-acoustic response due to hydrodynamic sources, *Computer Methods in Applied Mechanics and Engineering*, **190**, 345–361, (2000).

APPENDIX A

An incompressible flow description is obtained by integrating the reciprocal Biot-Savat induction of the two spinning vortices. The 2-D velocity field (u, v) induced by the two spinning vortex filaments is derived from the complex velocity potential: $u - iv = dw/dz$, where $z = x + iy$ is the complex coordinate. The complex velocity potential is $w(z) = \Phi + i\Psi$, where, Φ is the real velocity potential, and Ψ is the stream function. The resulting velocity potential due to the vortex n at the coordinate z_n is therefore:

$$w(z) = -\frac{i\Gamma}{2\pi}\Big\{ \log(z-z_n) - \log\big[z-(z_n+ih-2iy_1)\big] + $$
$$\log\big[z-(z_n-2ih)\big] - \ldots - \log\big[z-(z_n-ih-2iy_1)\big] + $$
$$\log\big[z-(z_n+2ih)\big] + \ldots \Big\}; \qquad (A.1)$$

where $\Gamma = 85$ m^{2}s^{-1} is the circulation of each vortex. The duct height $h = 1$ m and the density $\rho = 1.225$ kg/m^3 are used to normalize the other quantities. The vortex filaments are initially placed over the duct axis, separated by a distance $d = h/2$. The relevant velocity and Mach number are $U = \Gamma/d$ and $M = \Gamma/(dc_0) = 0.5$ with a speed of sound $c_0 = 340$ m/s. The velocity field and the wall pressure inside the duct, induced by the two spinning vortex filaments, is performed in two steps. In the first step, the trajectories of the two vortices are integrated in time, by evaluating the velocity field induced at each vortex position by the other filament. The velocity field over the whole duct domain can then be obtained from the complex potential induced by the two vortices at each time step. The ODE function of Matlab was used to solve the trajectory of the two vortices by time-marching the equations for the position of each vortex filament m, induced by its potential and the potential due to the other vortex n, accounting for their images:

$$u_m = -\frac{\Gamma}{4h}\left\{ \frac{\sin\left[\frac{\pi(y_m-y_n)}{h}\right]}{\cosh\left[\frac{\pi(x_m-x_n)}{h}\right] - \cos\left[\frac{\pi(y_m-y_n)}{h}\right]} + \right.$$
$$\frac{\sin\left[\frac{\pi(y_m+y_n)}{h}\right]}{\cosh\left[\frac{\pi(x_m-x_n)}{h}\right] + \cos\left[\frac{\pi(y_m+y_n)}{h}\right]} + $$
$$\left. \frac{\sin\left[\frac{2\pi y_m}{h}\right]}{1 + \cos\left[\frac{2\pi y_m}{h}\right]} \right\}; \qquad (A.2)$$

$$v_m = -\frac{\Gamma}{4h}\left\{ \frac{-\sinh\left[\frac{\pi(x_m-x_n)}{h}\right]}{\cosh\left[\frac{\pi(x_m-x_n)}{h}\right] - \cos\left[\frac{\pi(y_m-y_n)}{h}\right]} + \right.$$
$$\left. \frac{\sinh\left[\frac{\pi(x_m-x_n)}{h}\right]}{\cosh\left[\frac{\pi(x_m-x_n)}{h}\right] + \cos\left[\frac{\pi(y_m+y_n)}{h}\right]} \right\}; \quad (A.3)$$

for $m, n = 1, 2$ $(m \neq n)$. Integrating the unsteady Bernoulli equation:

$$\frac{\partial \Phi}{\partial t} + \frac{|V|^2}{2} + \int \frac{dp}{\rho} = 0. \qquad (A.4)$$

Along each wall, yields the unsteady pressure distribution at the wall, which is related to the local value of the velocity potential and slip velocity:

$$p_w = -\rho\left(\frac{\partial \Phi_w}{\partial t} + \frac{u_m^2}{2} \right). \qquad (A.5)$$

Once the kinematics of the vortices have been integrated, the velocity field at any point within the duct, except at the filament position, can be obtained from the summed velocity potentials of the vortices (A.1) with $n = 1, 2$. At every time step, velocity fields corresponding to the azimuthal velocity within a core size δ from the vortex filament considered as:

$$u = -\frac{\Gamma}{2\pi}\frac{y}{x^2 + y^2 + \delta^2}; \quad v = \frac{\Gamma}{2\pi}\frac{x}{x^2 + y^2 + \delta^2}. \quad (A.6)$$

The core sizes are kept small compared to the distance between the vortices to be consistent with filament-based mutual induction model, therefore it is considered to be equal to $\delta = h/50$.